



Research Paper

Numerical analysis and experimental validation of heat transfer characteristic for flat-plate solar air collector

Tzu-Chen Hung^{a,*}, Tsung-Jie Huang^b, Duen-Sheng Lee^c, Chih-Hung Lin^d, Bau-Shei Pei^b, Zeng-Yao Li^e^a Department of Mechanical Engineering, National Taipei University of Technology, Taiwan^b Department of Engineering and System Science, National Tsing Hua University, Taiwan^c Graduate Institute of Mechanical and Electrical Engineering, National Taipei University of Technology, Taiwan^d Center for Energy and Environmental Research, National Tsing Hua University, Taiwan^e Key Laboratory of Thermo-Fluid Science and Engineering, Ministry of Education, School of Energy and Power Engineering, Xi'an Jiaotong University, China

HIGHLIGHTS

- Various types of solar air collectors are discussed.
- CFD has been used to validate the characteristics of heat transfer.
- Solar Ray Tracing has been successfully used for thermal radiation flux.

ARTICLE INFO

Article history:

Received 20 March 2016

Revised 25 August 2016

Accepted 21 September 2016

Available online 22 September 2016

Keywords:

Solar chimney

Solar collector

CFD

Solar Ray Tracing

ABSTRACT

This study combines both concepts of solar ventilation technology and solar air collector. This is a quite innovative and potential facility to effectively use thermal energy and reduce the accumulation of heat in the indoor space simultaneously. The purpose of this study is to create a prototype and implement the experiments. Computational fluid dynamics (CFD) approach is employed to validate the characteristics of the flow and heat transfer. For the accuracy of numerical predictions, the method of Solar Ray Tracing was used for thermal radiation flux as boundary condition on the wall. The local heat transfer correlation was investigated to predict surrounding wind speed upon device cover. Three sorts of glasses and several aspect ratios of flow channels have been compared to conclude the optimal configuration. In addition, four important factors, such as the stagnant layer thickness, emissivity on the illustrated surface, mass flow rate and the height of the device, are also considered and discussed in detail. The result showed that the optimal design is dominated by the combination of an aspect ratio of 50 mm:10 mm, and appropriate mass flow rate to the height of the device. The present work on thermal energy collection can assist us in designing a powerful solar air collector in some potential applications.

© 2016 Elsevier Ltd. All rights reserved.

1. Introduction

Recently, overuse of fossil energy and carbon dioxide emissions has been increasing serious problems. Solar ventilation utilizes solar radiation energy to accumulate stack pressure, thus driving airflow through the flow channel. It has been widely applied in many different places such as solar chimney [1–3]. Solar chimney has become a feasible methodology for reducing energy consumption in building, Trombe wall [4] is applied to improve indoor thermal comfort during summer or winter, solar-energy drying [5,6], solar air conditioning [7] and power generation [8–10]. There have

thus far been relatively less researches, in which collecting the solar thermal energy from the concept of solar chimneys for electricity generation via organic Rankine cycles (ORC) [9]. This is an innovation approach for the application of solar thermal energy. However, the efficiency and outlet temperature of collector still can further improved. The main purpose of this study is to collect the temperature of the heat and the efficiency of solar chimney as high as possible by numerical investigation.

The solar chimney is a system composed of a glass, absorber plate, air channel and insulating material. The thermal performance and indoor thermal comfort of solar chimney has been extensively studied by experimental and numerical investigations. Harris and Helwig [11] numerically design a solar chimney to induce ventilation in building. Computational Fluid Dynamics

* Corresponding author.

E-mail address: tchung@ntut.edu.tw (T.-C. Hung).

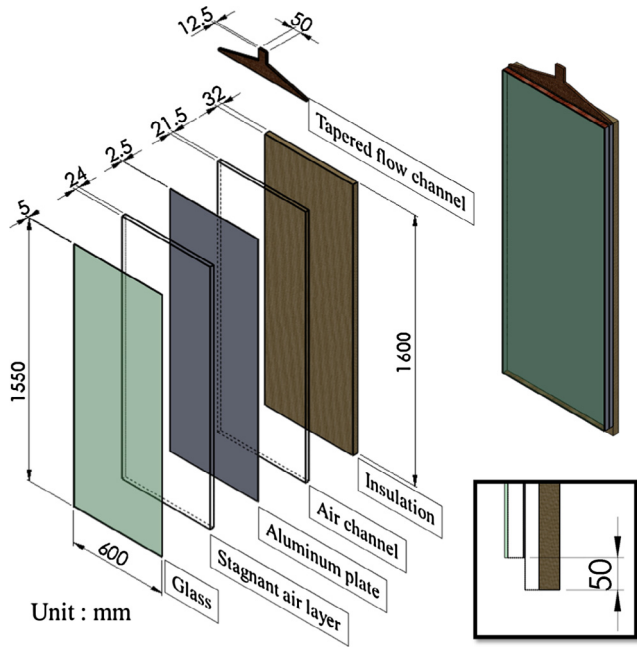


Fig. 1. The experiment components and their size.

The inlet and the exit of the air are located at the bottom and the top of the device, respectively. Inlet airflow was collimated by employing a laminated array to provide the velocity component in y-direction (vertical) only. Before conducting the performance tests, both the thermocouples and flow meters used were calibrated to ensure accurate measurements.

2.2. Mathematical models

CFD approach was used to perform the numerical calculations. The conditions in calculation domain are listed below:

- (1) Steady state,
- (2) Three-dimensional domain,
- (3) Low Mach number flow,
- (4) Fluid properties varied with temperature,

- (5) Turbulent flow,
- (6) Radiation effect.

The governing equations used are as follows:

Continuity equation:

$$\nabla \cdot (\rho \vec{v}) = 0 \quad (1)$$

Momentum equation:

$$\nabla \cdot (\rho \vec{v} \vec{v}) = -\nabla p + \rho \vec{g} + \mu \nabla^2 \vec{v} \quad (2)$$

Energy equation:

$$\nabla \cdot (\rho c_p T) = -\nabla \cdot (k_{eff} \nabla T) + S \quad (3)$$

Due to the range of Reynolds number, $60 \leq Re_D \leq 2450$, in the air channel, the flow phenomenon is slightly more than the upper limit of laminar phenomenon. In addition, the flow of stagnant air layer is unstable. Based on the reason above, the turbulent model should be used. However, the emphasis in this study is the effect of thermal radiation rather than the flow phenomenon. From the viewpoint of engineering, the general standard $k - \epsilon$ model with enhanced wall treatment is enough to estimate the heat transfer effect.

Turbulent kinetic energy equation:

$$\nabla \cdot (\rho k \vec{v}) = \left(\mu + \frac{\mu_t}{\sigma_k} \right) \nabla^2 k + G_k + G_b - \rho \epsilon \quad (4)$$

Turbulent dissipation equation:

$$\nabla \cdot (\rho \epsilon k \vec{v}) = \left(\mu + \frac{\mu_t}{\sigma_\epsilon} \right) \nabla^2 \epsilon + C_{1\epsilon} \frac{\epsilon}{k} (G_k + G_{3\epsilon} G_b) - C_{2\epsilon} \rho \frac{\epsilon^2}{k} \quad (5)$$

The radiative transfer equation without scattering consists of radiation intensity I , absorption coefficient a , refractive index n , Stefan-Boltzmann constant σ and local temperature T can be written as:

$$\nabla \cdot I + aI = an^2 \frac{\sigma T^4}{\pi} \quad (6)$$

To simulate solar heat flux, the solar load model was employed. Solar load model provides the position of solar, the direct solar irradiation and diffusive solar irradiation. It is a function to add heat source upon opaque and semi-transparent material. When

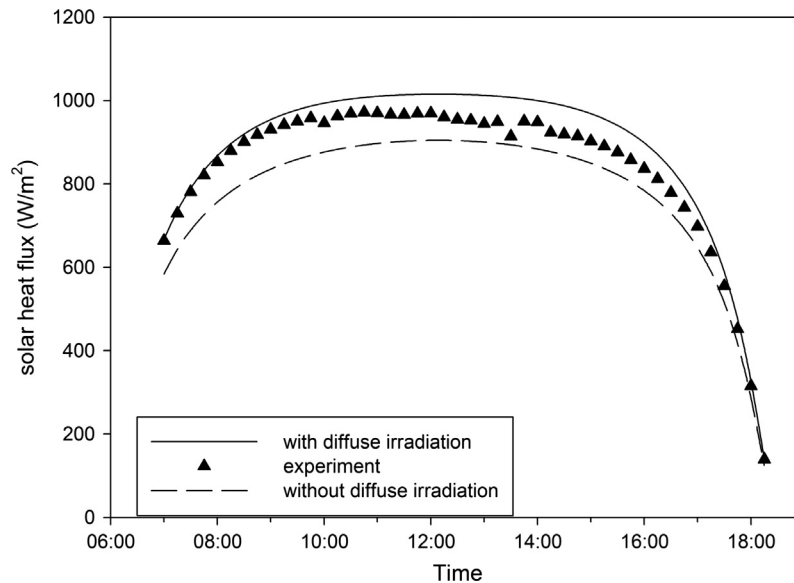


Fig. 2. The comparison of direct normal insolation.

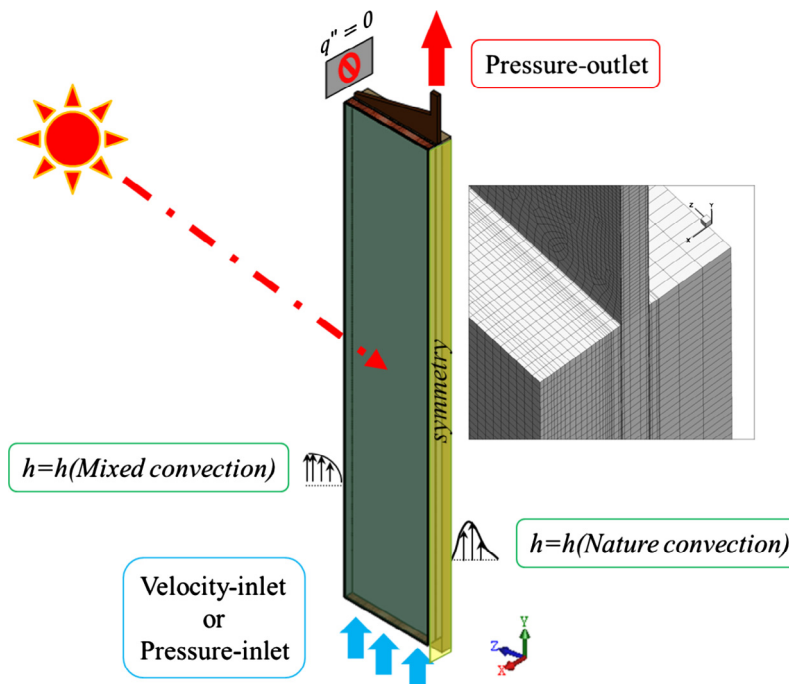


Fig. 3. The geometry, mesh and boundary conditions.

time and position of device are given, solar calculator would calculate the solar position vector and surface normal vector which is illuminated. Then separate the solar heat according to the transmittance and absorptance of the material and add the heat source in energy equation. Because the calculating form is not a kind of surface boundary conditions such as uniform heat flux, it will not conflict with the boundary conditions upon the glass.

Table 1
Properties of solid material.

	ρ (kg/m ³)	C_p (J/kg-K)	k (W/m-K)
Glass	2500	750	1.4
Aluminum plate	2700	896	167
Fireproof board	322	1800	0.039
Bakelite	640	1190	0.094

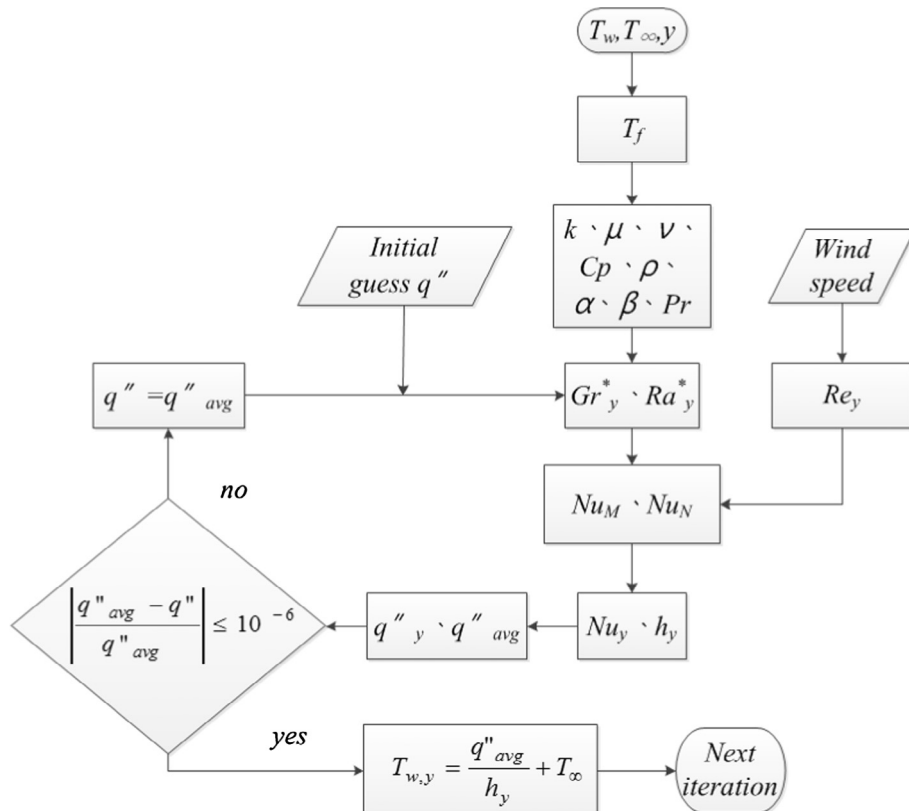


Fig. 4. The iterating process of local heat transfer.

Table 2
Radiative properties of green glass.

Glass	τ (–)	α (–)	ρ (–)	n (–)	ε (–)	a (1/m)	s (m)
Visible light	0.77	0.15	0.08	1.5	0.84	74.172	0.005
Infrared	0.48	0.46	0.08				

Table 3
The measuring instrument used in the experiments.





Instrument	Thermocouple (T-Type)	Air velocity transmitter	Pyranometer	Wind monitor
Image				
Output signal	Voltage (V)	Voltage (V)	Voltage (V)	Frequency (Hz)
Output physical quantities	Temperature (°C)	Velocity (m/s)	Solar radiation (W/m ²)	Velocity (m/s)
Range	–200 to 400 °C	0–10 m/s	0–2000 W/m ²	0–100 m/s
Accuracy	±0.5 °C	±0.2 m/s +3%	±2%	±0.3 m/s

Table 4
The detail of experiment.

θ (°)	v_{in} (m/s)	T_{∞} (°C)	v_{∞} (m/s)	Direct normal insolation (W/m ²)
20	4	37.44	1.85	983.6264

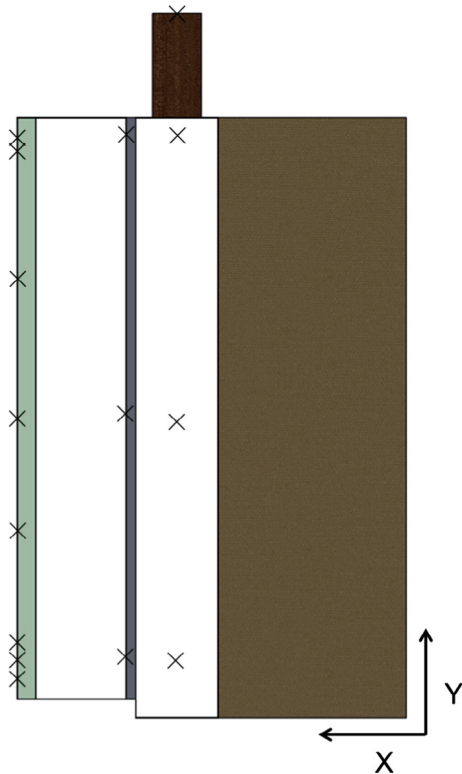


Fig. 5. The position of thermal couple upon the glass, upon the aluminum plate and in the air channel (with 10 times of scale in x-direction).

The solar load model has been validated below. Fig. 2 shows the measured direct normal insolation is between the curve with and without the diffuse irradiation in CFD. The so-called diffuse irradiation is consisting of the diffuse sky radiation and the solar radiation reflected from surrounding surfaces. This figure shows the upper and lower limits of real direct normal isolation and it is denote the solar load model is valid. However, the following

analysis does not contain the diffuse irradiation because it is difficult to determine.

The geometry, mesh and boundary conditions are shown in Fig. 3. The symmetric condition was employed in the middle of device. Velocity-inlet or pressure-inlet at inlet is set as with or without the fan, respectively. The side of the device was set to be adiabatic. The surface below the insulator was set to be local heat transfer with nature convection. However, the surface upon the glass was set to be local heat transfer with mixed convection because of the significance of environmental wind speed. The geometry is divided into 1,235,850 hexahedral meshes. The mesh size of height and width is 3.875 mm and 4 mm, respectively. Further, the mesh size of the thickness for air channel and the stagnant air layer is 1.15 mm and 1.85 mm, sequentially. Because of the enhanced wall treatment employed, the fluid mesh adjacent to solid wall was refined to ensure $y_{avg}^+ \leq 1$.

2.3. Calculation of local heat transfer coefficient

Because of the complicated situation around the environment, the heat transfer coefficients upon glass and behind insulation layer are considered carefully. To make environmental convection more accurate, the local heat transfer under various heights are applied in boundary condition upon the glass and behind the layer of insulation instead of the constant heat transfer coefficient. The correlation of mixed convection is combined with forced convection and natural convection as given in Eqs. (7)–(9). The Nusselt number of mix convection is given [23]:

$$Nu_y = (Nu_{y,F}^3 + Nu_{y,N}^3)^{1/3} \quad (7)$$

The Nusselt number of forced convection is [24]:

$$Nu_{y,F} = C_1 Re_y^n Pr^{1/3} \quad (8)$$

where $C_1 = 0.453$, $n = 1/2$ for laminar; $C_1 = 0.030784$, $n = 4/5$ for turbulent. The Nusselt number of natural convection is [25]:

$$Nu_{y,N} = C_1 \left(\frac{Ra_{y,0}^* Pr}{C_2 + Pr} \right)^n \quad (9)$$

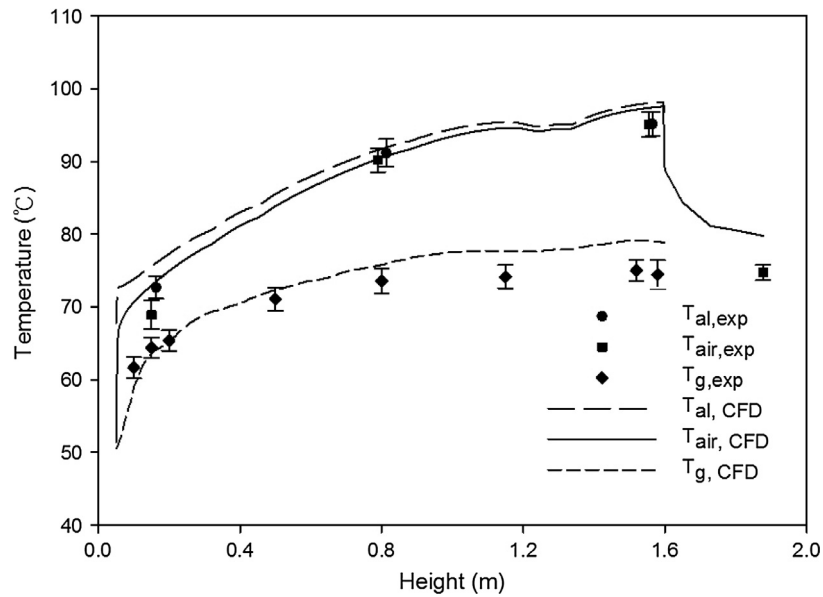


Fig. 6. Temperature varied with height for glass, aluminum plate and air channel.

Table 5

The error in the glass, aluminum plate and air channel.

	Mean error (%)	Max. error (%)
Glass	6.74	12.03
Aluminum plate	5.74	10.32
Air channel	7.82	13.49

where $C_1 = 0.630$, $C_2 = 0.670$, $n = 1/5$ for laminar; $C_1 = 0.219$, $C_2 = 0.191$, $n = 1/4$ for turbulent.

The calculation procedures are shown in Fig. 4 and list below:

1. Calculate the properties which depend on temperature;
2. Calculate Gr_y^* and Ra_y^* by using initial guess of q'' ;
3. Calculate Re_y by using wind speed;
4. Determine the local heat transfer;
5. Average the q''_y to get q''_{avg} ;
6. Check if $q'' \approx q''_{avg}$;

7. If not, let $q'' = q''_{avg}$ and continue calculating;

8. If yes, then go for next iteration.

When the above procedures are completed, the local heat transfer is clearly determined and the temperature on the glass will be more accurate than set the constant heat transfer coefficient at boundary.

2.4. Material properties

The properties of solid material are list in Table 1. Among them, fireproof board is for insulation material, and bakelite is used to make tapered flow channel. The radiative properties of green glass used for validation are listed in Table 2. The absorption coefficient is calculated by Eq. (10).

$$a = \frac{1}{s} \ln \left(\frac{B + \sqrt{A^2 + B^2}}{A} \right) \quad (10)$$

where $A = 2 \tau$, $B = (1 - \rho)^2 - \tau^2$ [26,27].

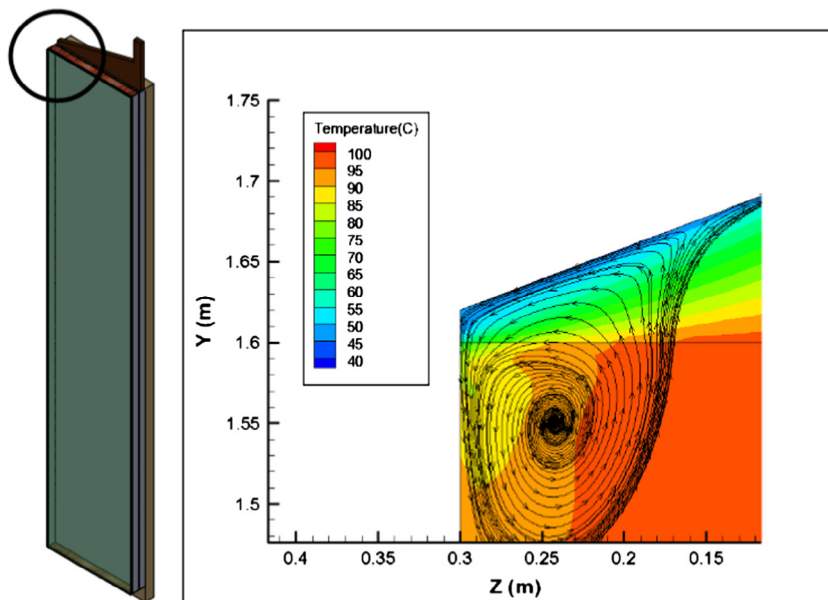


Fig. 7. The temperature contour and flow field of tapered flow channel.

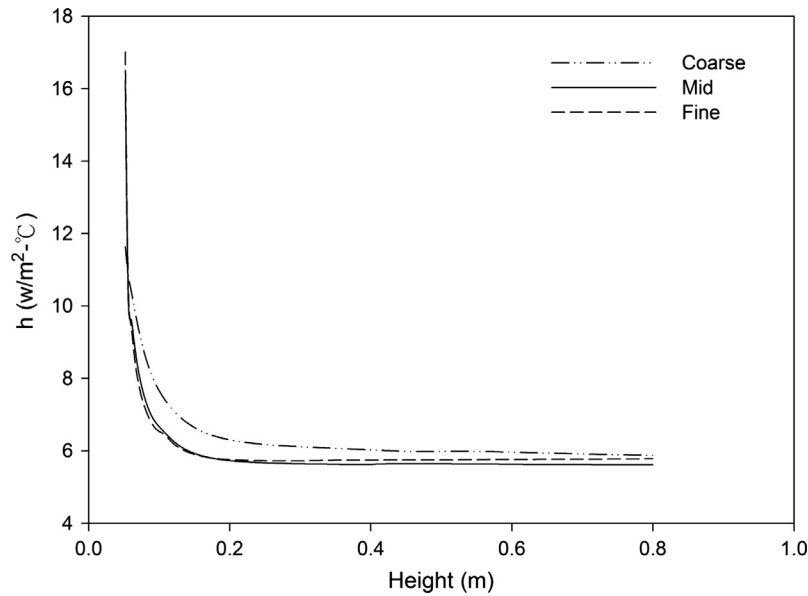


Fig. 8. Local heat transfer coefficient vary with height.

Table 6

The scale of turbulent thermal conductivity at different surface.

The surface varying at x-direction	$k_t/k_{eff} \times 100\%$
Between glass and stagnant air layer	1.663×10^{-6}
Between stagnant air layer and aluminum plate	9.580×10^{-7}
Between aluminum plate and air channel	2.104×10^{-7}

Table 7

The transmittance and absorptance of three types of glass.

Optical properties	Visible		Infrared	
	τ_V	α_V	τ_{IR}	α_{IR}
Super clear	0.91	0.01	0.89	0.03
Clear	0.89	0.03	0.81	0.12
Green	0.77	0.15	0.48	0.46

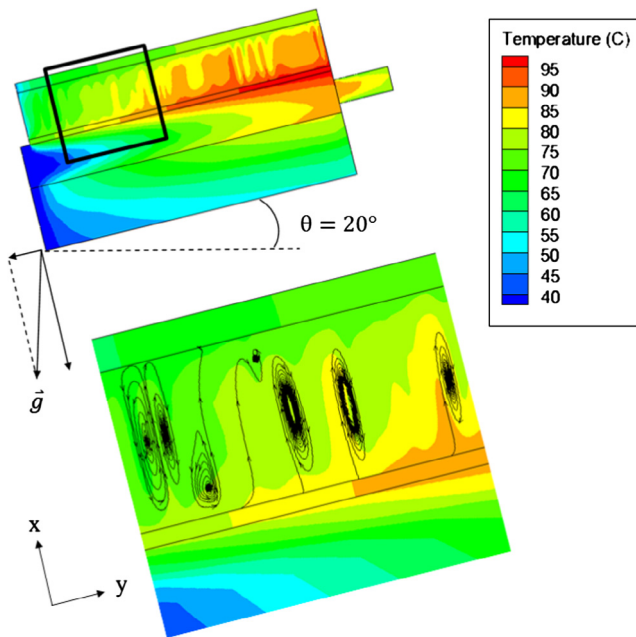


Fig. 9. The temperature contour under natural convection for x-y plane at $z=0$ (with 10 times of scale in x-direction).

2.5. Benchmark

The experiment data were measured once every minute on 26 Aug. 2014, started from 6:45 and ended at 17:45 on the campus of National Taipei University of Technology. In the experiment, the measuring instruments have been calibrated in order to reduce

measurement errors. Details of the measuring instruments used are shown in Table 3. To reduce the influence from environment, the data collection runs from 11:00 A.M. to 12:00 A.M. The related detail of environmental conditions and the setup of experiment device are shown in Table 4. And the position measuring is shown in Fig. 5, which is magnified 10 times of scale in x-direction.

To validate CFD results, experimental investigations were performed outside. Fig. 6 shows the temperature of glass, aluminum plate and air channel at different height including not only experimental but also the results from numerical simulations. The uncertainty is calculated and presented as error bar [28]. Further, the main sources of uncertainty included the accuracy of the instrumental measurements such as thermocouple ($\pm 0.5^\circ\text{C}$), the Instrument Repeatability ($\pm 1.3^\circ\text{C}$), the ambient temperature ($\pm 0.4^\circ\text{C}$), and the solar heat flux ($\pm 0.3^\circ\text{C}$), etc.

The maximum error and average error of glass, aluminum plate and air channel is list in Table 5, in which the error is calculated by Eq. (11). To make the results more practical, the experiment is at outdoor instead of at indoor. Therefore, the tapered flow channel is used to avoid the environment wind affect the flow field of outlet. Although the tapered flow channel is covered by insulation, there still many energy dissipate. Fig. 7 shows the flow field in the tapered flow channel. Hot air is cooled and then forms a vortex at the corner resulting more cooled air. This physical phenomena cause a sharp temperature decrease when height over 1.6 m in Fig. 6.

$$E = \left| \frac{T_{EXP} - T_{CFD}}{T_{EXP} - T_{\infty}} \right| \times 100\% \quad (11)$$

Fig. 8 shows the variation of local heat transfer coefficient defined by Eq. (12) with height until 0.8 m. The mesh numbers of coarse, mid and fine mesh are 765,430, 1,235,850 and 2,723,150,

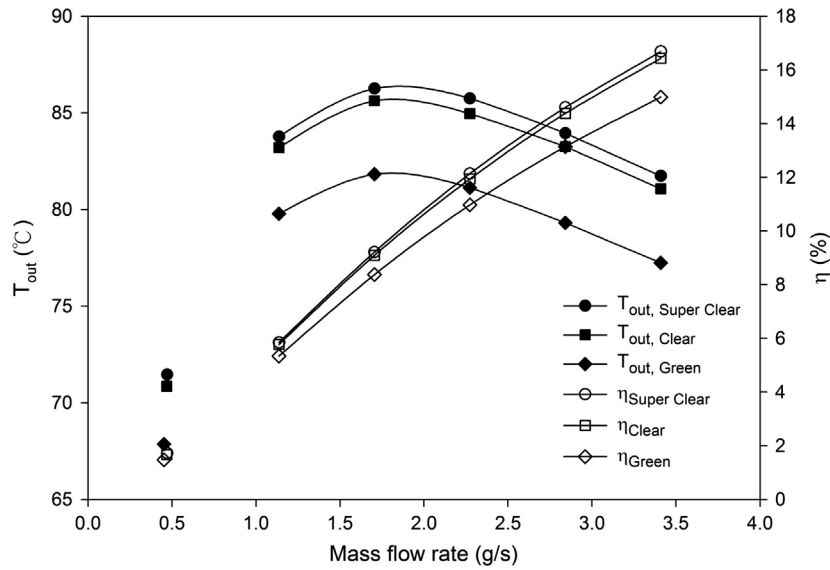


Fig. 10. Variation of temperature rise and efficiency with mass flow rate for different types of glass.

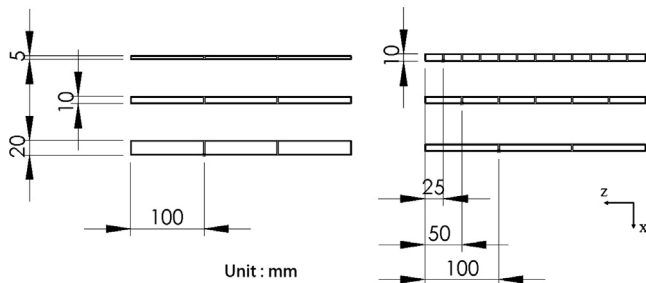


Fig. 11. The cross section and associate size of rectangular-tube.

respectively. All three cases apparently vary in the beginning 0.2 m. It is clearly shown that mid mesh is closer to fine mesh than coarse mesh. To get balance between accuracy and calculation time, we use mid mesh for the following parametric research.

$$h = \frac{q''_w}{T_w - T_b} \quad (12)$$

Table 6 shows the ratio of the turbulent conductivity, in which the effective conductivity is shown in Eq. (13) and determined by Eqs. (14) and (15). The value of constants Pr_t is 0.85 and C_μ is 0.09, respectively. It can be seen that its proportion is very small. It means that employing more accurate turbulent model is not necessary. Although the influence of the turbulent model will not make too much difference, we still employ the turbulent model to ensure the correctness of physical phenomena.

$$k_{eff} = k_f + k_t \quad (13)$$

$$k_t = \frac{c_p \mu_t}{Pr_t} \quad (14)$$

$$\mu_t = \rho C_\mu \frac{k^2}{\varepsilon} \quad (15)$$

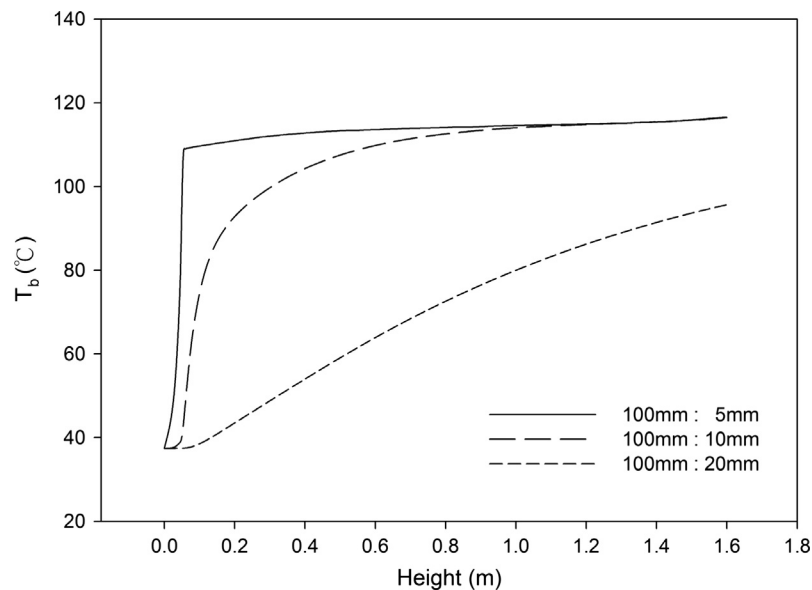


Fig. 12. The bulk temperature versus height at different aspect ratio of flow section along y-direction for width of 100 mm.

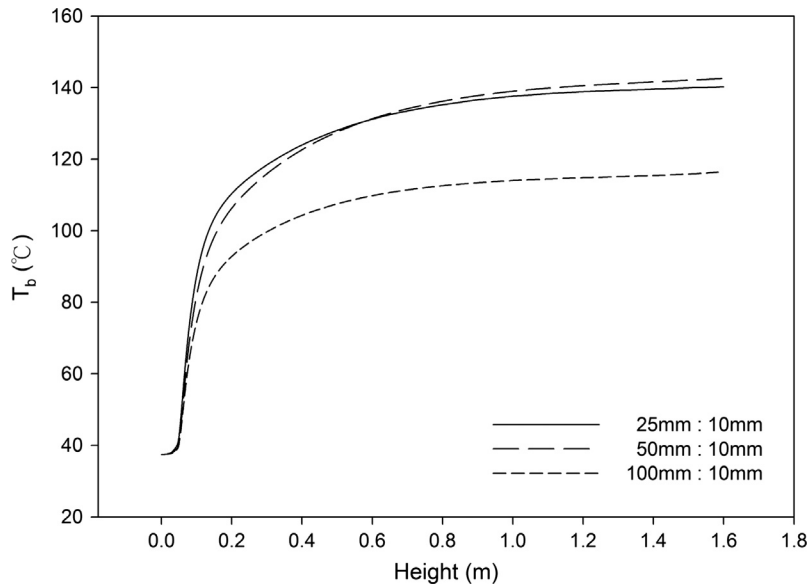


Fig. 13. The bulk temperature versus height at different aspect ratio of flow section along y-direction for the depth of 10 mm.

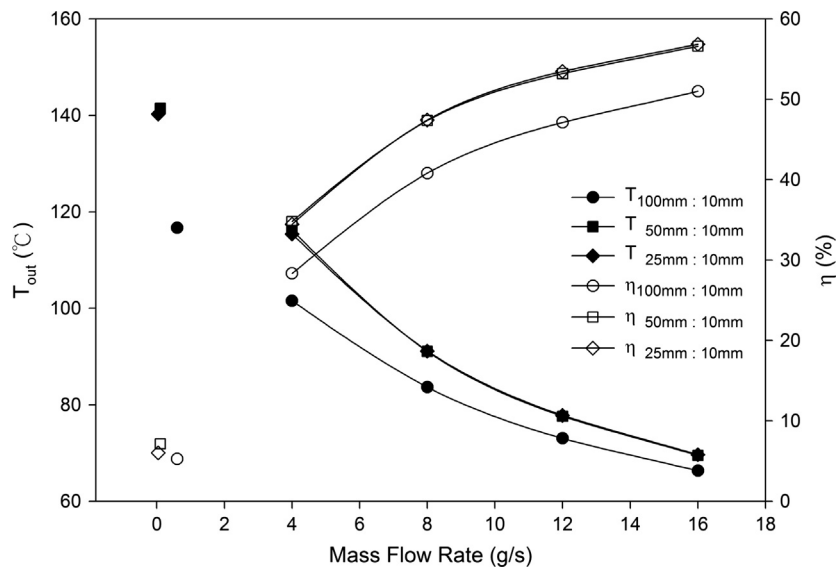


Fig. 14. Outlet temperature and efficiency versus air flow rate for three aspect ratios of flow channel.

Fig. 9 shows the temperature contour under natural convection for x-y plane at $z = 0$, in which the x-direction is magnified 10 times to comfortably observe the phenomena. As can be seen, the thermal boundary layer is clear on the wall of the air channel. The stagnant air layer has circular flow field because of the effect of gravity. The temperature of insulation layer varies violently because of its low thermal conductivity. It is confirmed that the results from CFD tool is credible.

3. Numerical results and discussions

The default setup is list below if the setting is not specifically mentioned. Solar heat flux $q''_s = 1000 \text{ W/m}^2$, inclined angle $\theta = 20^\circ$, height $H = 1.6 \text{ m}$, emissivity on heating surface $\varepsilon = 1$, stagnant air layer thickness $\delta = 24 \text{ mm}$, ambient temperature $T_\infty = 37.4^\circ\text{C}$, ambient wind speed $v_\infty = 1.85 \text{ m/s}$, and super clear glass is used.

3.1. Effect of glass sort

To understand the effect of different glass, three sorts of glass naming green, clear and super clear with the optical properties as listed in Table 7 are applied. The definition of efficiency is written as Eq. (16), where the width $Z = 0.6 \text{ m}$. As shown in Fig. 10, the results are for the boundary conditions on the right and left hand sides, which are nature convection and mixed convection, respectively, as that shown in Fig. 3. It indicates that higher the transmittance, higher the outlet temperature and efficiency. Because high transmittance results in more heat absorption by the collector, the outlet temperature and efficiency is raised.

$$\eta = \frac{\dot{m}c_p(T_{out} - T_\infty)}{q''_s Z H} \quad (16)$$

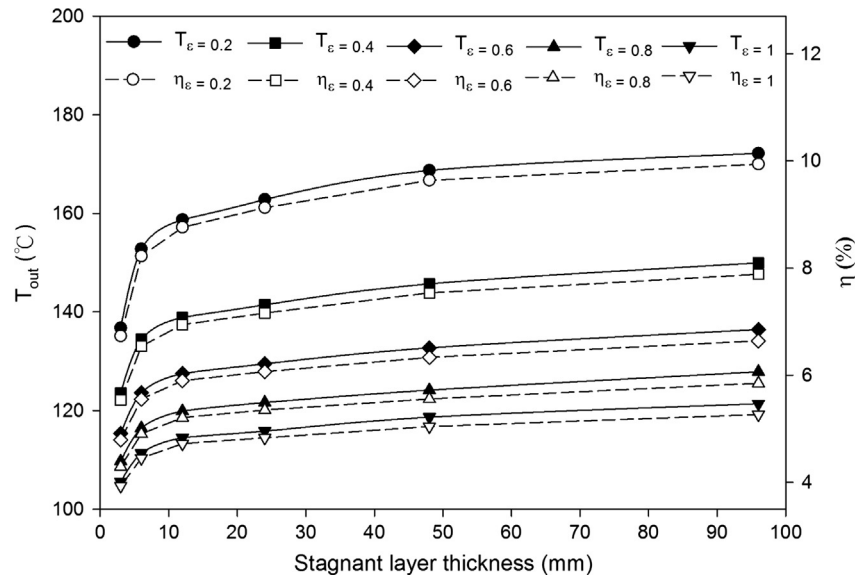


Fig. 15. Outlet temperature and collect efficiency versus stagnant air layer thickness at different emissivity for natural convection.

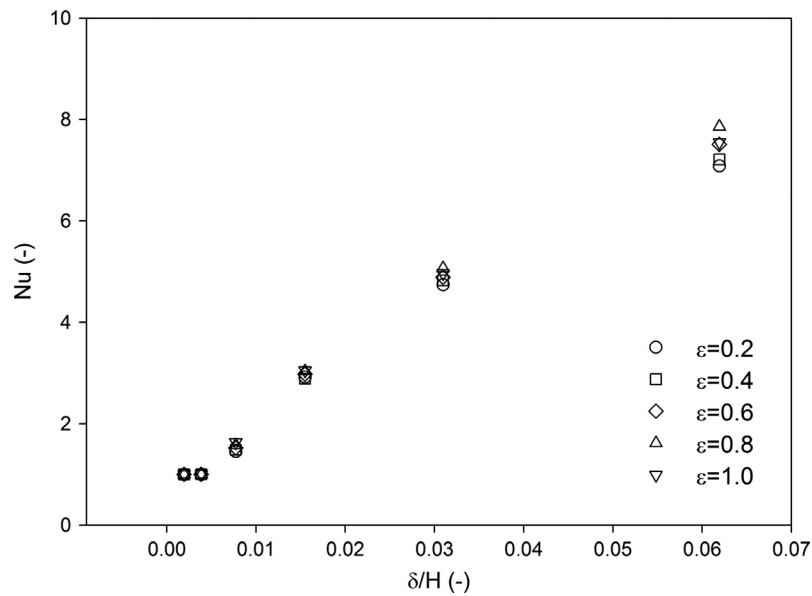


Fig. 16. Nusselt number versus δ/H at different emissivity on metal plate.

3.2. Effect of chimney type

First of all, the effect under natural convection was implemented. To enhance the achievement of device, the geometry of the air collector channel was modified from plate to rectangular tube as shown in Fig. 11. Because of more contact area with fluid, the rectangular-tube air flow channel results in higher outlet temperature and efficiency. As shown in Fig. 12, here are the results of the cross-section bulk temperatures varying along y-direction, at natural convection with different aspect ratio. Referring to Fig. 11, the aspect ratio represents the ratio of width to depth of the metal tube. The bulk temperature increases faster at entrance region when aspect ratio is greater, but it is hard to keep the gradient to make temperature higher thereafter.

Fig. 13 also shows greater bulk-temperature gradient around entrance by varying the collector aspect ratio for the same depth of 10 mm. The configuration is also referred to Fig. 11. Small flow

section area makes temperature increase too rapid so that the solar heat can hardly be absorbed downstream. It is shown that the smaller the x or z-direction length is, the faster the temperature varies along the stream, and the faster the temperature gradient slow down along y-direction.

Since the flow is not smooth and the air could be confined within the flow channel, we considered to provide weak force flow by consuming very small amount of electricity to guide the air flow. Therefore, we installed suction fan at the inlet of the device to provide and control mass flow rates.

Fig. 14 shows the outlet temperature and efficiency under different mass flow rate with the same group of preceding three aspect ratios. When the aspect ratio is changed from 100 mm:10 mm to 50 mm:10 mm, the outlet temperature is reduced and the efficiency is retained the same tendency of increase under growing mass flow rate. But when the aspect ratio is replaced from 50 mm:10 mm to 25 mm:10 mm, both the

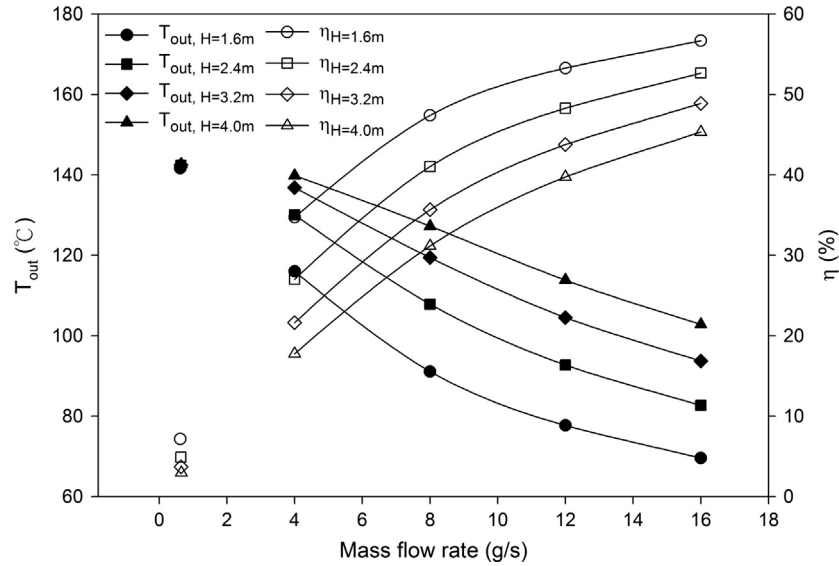


Fig. 17. The outlet temperature and efficiency versus mass flow rate at different height of the device.

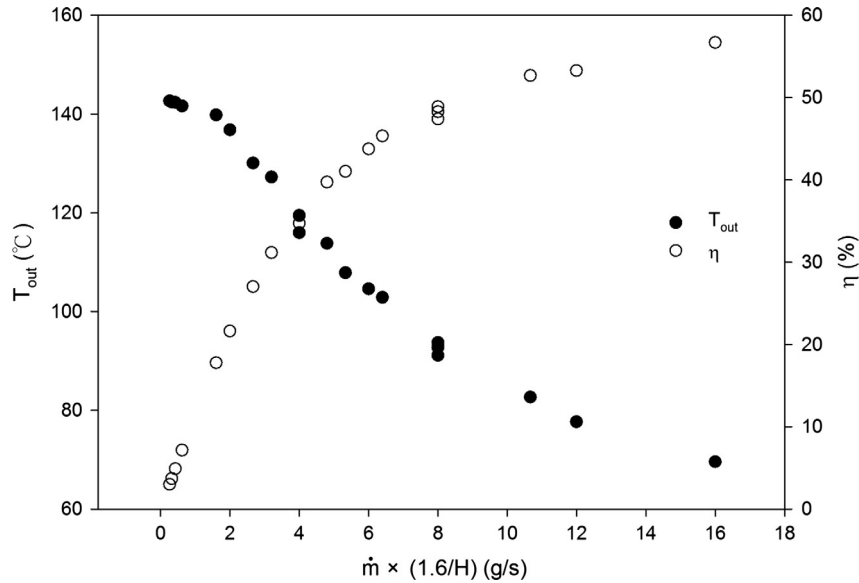


Fig. 18. The outlet temperature and efficiency versus normalized mass flow rate.

efficiency and outlet temperature are almost the same under growing mass flow rate. This represents the narrow channel is positive, but too narrow could have an opposite effect.

This figure clearly shows that the type of rectangular tube is better than that of plate channel. But the best one would be neither the smallest flow section nor the extremely big or small aspect ratio. Among them, the rectangular tube with the aspect ratio of 50:10 performs the best, the discussion below will employ this ratio to implement the parametric analyses.

3.3. Effect of emissivity on heating surface

Fig. 15 shows the outlet temperature and efficiency versus the stagnant layer thickness at different emissivity on heating surface of metal plate under natural convection. As can be seen, the thicker stagnant layer makes higher thermal resistant between heating surface and glass. Because of this, the outlet temperature and

collect efficiency will increase when the stagnant layer is growing up. Moreover, lower emissivity makes less thermal radiation dissipation. It results in higher outlet temperature and efficiency as well. Consequently, thicker stagnant layer and lower emissivity would be better. For practical purpose, 24 mm thickness of stagnant layer is more appropriately.

Fig. 16 shows the Nusselt number versus δ/H at different emissivity on heating surface. As can be seen in the figure, Nusselt number is very close to 1 when δ/H is small. By definition, $Nu = 1$ means that heat conduction is the dominant heat transfer mechanism. It will dissipate more heat when stagnant layer thickness is thinner. Consequently, the outlet temperature drops a lot when stagnant layer thickness is small to make Nusselt number near 1. In which the Nusselt number in stagnant layer is defined as [24]:

$$Nu_{\delta} = \frac{q_{\delta}}{k(T_{al} - T_g)} \quad (17)$$

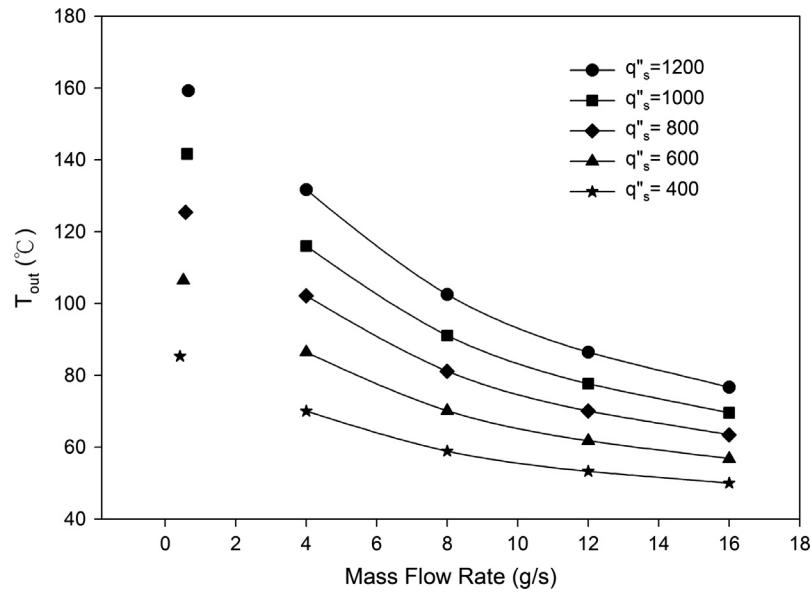


Fig. 19. The outlet temperature versus mass flow rate at different solar heat flux.

3.4. Effect of height

Since the pure natural convection cannot efficiently collect the solar heat, a weak forced flow to guide air flow was adopted. Fig. 17 shows the outlet temperature and efficiency versus mass flow rate for different height of the devices. As can be seen, heightening device is able to raise outlet temperature but the efficiency would be decreased. Since the heightening device has more heating surface area, the outlet temperature is increased because the air molecules have longer residence time. On the other hand, higher dissipation of thermal radiation results in a lower efficiency. But when mass flow rate is increased, the variation of outlet temperature and efficiency is different. The reduced contact time between surface and the fluid from the increase of mass flow rate causes a decrease in outlet temperature and an increase in efficiency. Based on the above mentioned, the opposite tendency of

increasing height and mass flow rate is observed. This points the parameter combined with the preceding two parameters may exist.

Because a regular tendency in Fig. 17 is observed, Fig. 18 shows that both the outlet temperature and efficiency are function of the normalized mass flow rate. As the mass flow rate times a dimensionless number (1.6 m/H), all four curves become one curve including not only outlet temperature but also efficiency.

3.5. Effect of solar heat flux

Fig. 19 shows when the collector is heated by higher solar heat flux, higher the outlet temperature is induced. Fig. 20 shows that the efficiency in heat collection is almost independent of the change of solar heat flux. It is because the efficiency is proportional to the average internal heat transfer coefficient h_{avg} , which is

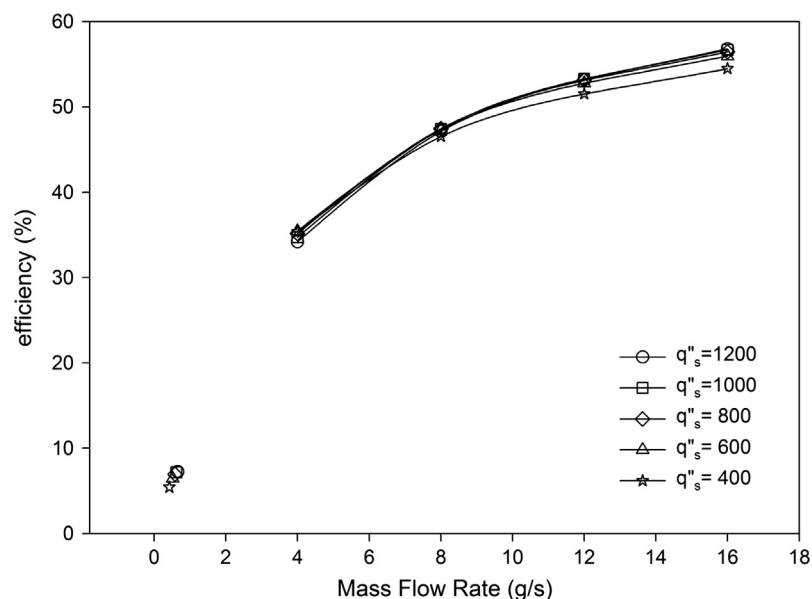


Fig. 20. The efficiency versus mass flow rate at different solar heat flux.

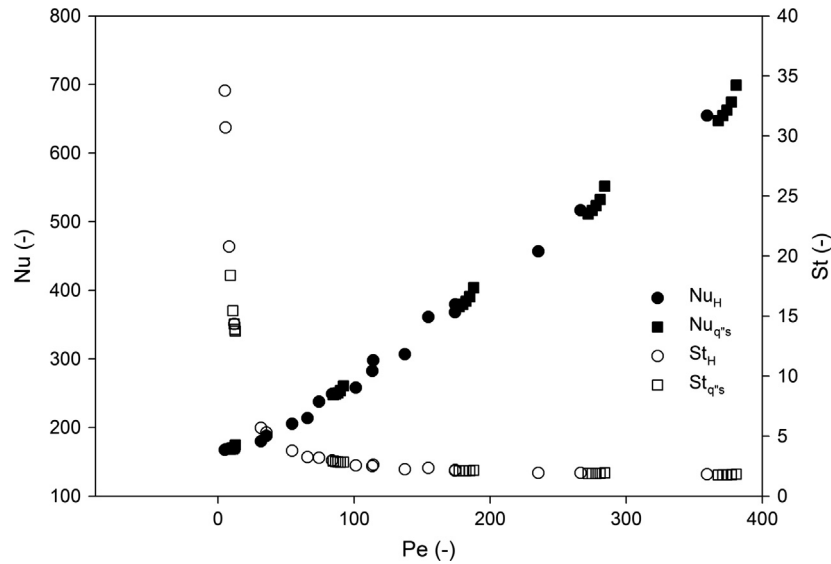


Fig. 21. Nusselt number and Stanton Number versus Peclet number under the conditions of $\theta = 20^\circ$, super clear glass, rectangular flow section 50 mm:10 mm, $q''_s = 400\text{--}1200\text{ W/m}^2$, and $H = 1.6\text{--}4.0\text{ m}$.

dependent of the inlet velocity instead of the wall heat flux. Where the correlation $Nu = CRe^n Pr^m$ is usually used to represent the convective heat transfer in internal flow. No matter how, the stronger forced guide flow, the efficiency is enhanced in heat collection.

3.6. Dimensionless number

Fig. 21 shows the Nusselt number and Stanton number vary with Peclet number. The conditions are at the inclination angle of $\theta = 20^\circ$, super clear glass, rectangular flow channel section 50 mm:10 mm, $q''_s = 400\text{--}1200\text{ W/m}^2$, $H = 1.6\text{--}4.0\text{ m}$. The definition of dimensionless numbers are list below, where $Z = 0.6\text{ m}$. The grow-up of Nusselt number means more heat would be collected at outlet due to the higher inlet velocity. Moreover, the sharp down of Stanton number means the mechanism of heat transfer is dominate not by temperature difference, but the enhanced inlet velocity. Eq. (21) indicates the relation between Stanton number and efficiency. It is indicated that if we want to get higher efficiency in heat collection, greater inlet velocity is definitely the best way. Further studies for wider aspect ratio, inclined angle from horizontal, etc. are encouraged to be completed for a better form of correlation like that of Fig. 20.

$$Pe = \frac{\dot{m}}{\mu H} \frac{\nu}{\alpha} \quad (18)$$

$$Nu = \frac{q''_s Z}{k(T_{out} - T_\infty)} \quad (19)$$

$$St = \frac{Nu}{Pe} \quad (20)$$

$$\eta = \frac{1}{St} \times 100\% \quad (21)$$

4. Conclusion remarks

1. The higher the transmittance, the higher outlet temperature, the better efficiency.
2. The best aspect ratio of rectangular tube flow section is 50 mm:10 mm, which happens not only at nature convection but also at mixed convection.

3. The outlet temperature and efficiency are inversely proportional to the emissivity on heating surface.
4. Thicker stagnant layer is better, but 24 mm is a much suitable size.
5. A correlation has been established among the outlet temperature, efficiency, mass flow rate, and height.
6. The overall system behavior can be represented by Peclet number, Nusselt number and Stanton number under the conditions of inclined angle $\theta = 20^\circ$, using super clear glass, rectangular collector with flow cross section of 50 mm:10 mm, solar heat flux $q''_s = 400\text{--}1200\text{ W/m}^2$ and height $H = 1.6\text{--}4.0\text{ m}$.

Acknowledgements

The authors would like to acknowledge the Ministry of Science, Technology of the Republic of China for their financial supports for this research under Contract No. MOST 104-2221-E-027-087.

References

- [1] R. Khanal, C. Lei, Solar chimney—a passive strategy for natural ventilation, *Energy Build.* 43 (2011) 1811–1819.
- [2] A.P. Haghighi, M. Maerefat, Solar ventilation and heating of buildings in sunny winter days using solar chimney, *Sust. Cities. Soc.* 10 (2014) 72–79.
- [3] X.Q. Zhai, Z.P. Song, R.Z. Wang, A review for the applications of solar chimneys in buildings, *Renew. Sust. Energy Rev.* 15 (2011) 3757–3767.
- [4] X.Q. Hong, Wei He, Z.T. Hu, C.C. Wang, J. Ji, Three-dimensional simulation on the thermal performance of a novel Trombe wall with venetian blind structure, *Energy Build.* 89 (2015) 32–38.
- [5] A. Sharma, C.R. Chen, N.V. Lan, Solar-energy drying systems: a review, *Renew. Sust. Energy Rev.* 13 (2009) 1185–1210.
- [6] O.V. Ekechukwu, B. Norton, Review of solar-energy drying systems III: low temperature air-heating solar collectors for crop drying applications, *Energy Convers. Manage.* 40 (1999) 657–667.
- [7] A. Al-Alili, Y. Hwang, R. Radermacher, Review of solar thermal air conditioning technologies, *Int. J. Refrig.* 39 (2014) 4–22.
- [8] A. Zandian, M. Ashjaee, The thermal efficiency improvement of a steam Rankine cycle by innovative design of a hybrid cooling tower and a solar chimney concept, *Renew. Energy* 51 (2013) 465–473.
- [9] T.C. Hung, D.S. Lee, J.R. Lin, An innovative application of a solar storage wall combined with the low-temperature organic Rankine cycle, *Int. J. Photoenergy* (2014) 1–12.
- [10] J.C. Chang, C.W. Chang, T.C. Hung, J.R. Lin, K.C. Huang, Experimental study and CFD approach for scroll type expander used in low-temperature organic Rankine cycle, *Appl. Therm. Eng.* 73 (2014) 1444–1452.
- [11] D.J. Harris, N. Helwig, Solar chimney and building ventilation, *Appl. Energy* 84 (2007) 135–146.

- [12] J. Arce, M.J. Jiménez, J.D. Guzmán, M.R. Heras, G. Alvarez, J. Xamán, Experimental study for natural ventilation on a solar chimney, *Renew. Energy* 34 (2009) 2926–2934.
- [13] D.S. Lee, T.C. Hung, J.R. Lin, J. Zhao, Experimental investigations on solar chimney for optimal heat collection to be utilized in organic Rankine cycle, *Appl. Energy* 154 (2015) 651–662.
- [14] R. Bassiouny, N.S.A. Koura, An analytical and numerical study of solar chimney use for room natural ventilation, *Energy Build.* 40 (2008) 865–873.
- [15] K.E. Amori, S.W. Mohammed, Experimental and numerical studies of solar chimney for natural ventilation in Iraq, *Energy Build.* 47 (2012) 450–457.
- [16] B. Zamora, A.S. Kaiser, Optimum wall-to-wall spacing in solar chimney shaped channels in natural convection by numerical investigation, *Appl. Therm. Eng.* 29 (2009) 762–769.
- [17] J. Mathur, N.K. Bansal, S. Mathur, M. Jain, Anupma, Experimental investigations on solar chimney for room ventilation, *Sol. Energy* 80 (2006) 927–935.
- [18] J.J. Hu, X.S. Sun, J.L. Xu, Z.X. Li, Numerical analysis of mechanical ventilation solar air collector with internal baffles, *Energy Build.* 62 (2013) 230–238.
- [19] Y. Varol, H.F. Oztop, A comparative numerical study on natural convection in inclined wavy and flat-plate solar collectors, *Build Environ.* 43 (2008) 1535–1544.
- [20] S.V. Karmare, A.N. Tikekar, Analysis of fluid flow and heat transfer in a rib grit roughened, surface solar air heater using CFD, *Sol. Energy* 84 (2010) 409–417.
- [21] D. Dović, M. Andrassy, Numerically assisted analysis of flat and corrugated plate solar collectors thermal performances, *Sol. Energy* 86 (2012) 2416–2431.
- [22] W. Chen, W. Liu, Numerical analysis of heat transfer in a passive solar composite wall with porous absorber, *Appl. Therm. Eng.* 28 (2008) 1251–1258.
- [23] B.F. Armaly, T.S. Chen, N. Ramachandran, Correlations for laminar mixed convection on vertical, inclined and horizontal flat plates with uniform surface heat flux, *Int. J. Heat Mass Trans.* 30 (2) (1987) 405–408.
- [24] J.P. Holman, *Heat Transfer*, tenth ed., McGraw-Hill, New York, 2010.
- [25] O. Aydin, L. Guessous, Fundamental correlations for laminar and turbulent free convection from a uniformly heated vertical plate, *Int. J. Heat Mass Trans.* 44 (2001) 4605–4611.
- [26] V.P. Nicolau, F.P. Maluf, Determination of radiative properties of commercial glass, in: *The 18th International Conference on Passive and Low Energy Architecture*, Florianópolis, Brazil, 2001, pp. 759–764.
- [27] M. Rubin, Optical properties of soda lime silica glasses, *Sol. Energy Mater.* 12 (1985) 275–278.
- [28] R.S. Figliola, D.E. Beasley, *Theory and Design for Mechanical Measurements*, fifth ed., John Wiley & Sons, New York, 2011.